Research article

Carbon Future

Regulation of cobalt active sites by antimony to match adsorption configuration for propyne semihydrogenation

Xiaohu Ge[1], Ziyue Kou[1], Nina Fei[1], Yueqiang Cao[1]✉, Hao Jiang[2], Xinggui Zhou[1], and Xuezhi Duan[1]✉

[1] *State Key Laboratory of Chemical Engineering, East China University of Science and Technology, Shanghai 200237, China*
[2] *School of Materials Science and Engineering, East China University of Science and Technology, Shanghai 200237, China*

Cite This: *Carbon Future* **2024**, *1*, 9200020

Read Online

ABSTRACT: Designing and fabricating atomically uniform active sites toward favorable adsorption configuration of essential species to match specific reaction pathways is of great importance in catalytic semihydrogenations, yet it remains challenging. In this research, we present a straightforward method for synthesizing a CoSb intermetallic catalyst through the structural conversion of layered double hydroxide precursors, optimizing Co sites for configuration matching in propyne semihydrogenation. Characterizations using X-ray diffraction, high resolution transmission electron microscopy, and X-ray absorption spectroscopy demonstrate the formation of *P6$_3$/mmc* CoSb intermetallic phase. The CoSb intermetallic catalyst, with its well-organized atomic surface and optimized electronic structure, achieves 97.0% propylene selectivity with nearly complete propyne conversion. Temperature-programmed surface reaction and desorption measurements, along with theoretical calculations, unravel that this exceptional selectivity arises from the kinetically preferred desorption of propylene over its further hydrogenation to undesired propane byproduct on the finely regulated Co sites of the CoSb intermetallic catalyst.

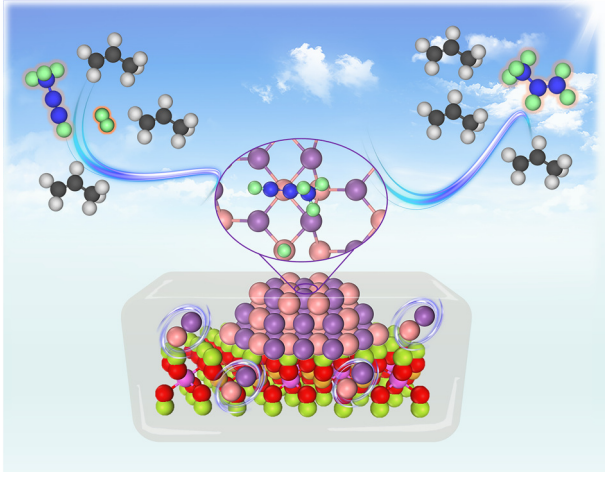

KEYWORDS: Propyne semihydrogenation, Co–Sb intermetallic, adsorption behavior, site isolation, propylene selectivity

1 Introduction

Heterogeneous catalysis for selective hydrogenations is a crucial reaction with wide-ranging industrial and synthetic applications, ranging from bulk to fine chemicals. A key example is the selective hydrogenation of propyne in excess propylene, which is essential for purifying propylene produced from naphtha steam cracking and propane dehydrogenation[1–3]. Although Pd-based catalysts are highly efficient for this reaction due to their optimal d-band width and are highly regarded in both academia and industry[4, 5], the scarcity and high cost of precious Pd highlight the need for improving scalability and cost-effectiveness in catalyst design and practical applications. To address this, significant efforts have been dedicated to the development of more cost-effective catalysts. Strategies include (i) reducing the amount of noble metals through the "active-site isolation" strategy or minimal ensemble engineering[6–9], and (ii) developing well-defined and stable site-isolated nonnoble-metal-based catalysts[10, 11].

Introducing a guest metal to bond with an isolated host metal site is a common strategy for precisely tuning the configurations of essential species to enhance selectivity toward desired products[5, 12–15]. Recently, intermetallic catalysts featuring stable, long-range ordered structures have emerged as promising candidates for selective propyne hydrogenation. By modulating the host active metal (e.g., Pd[9, 16, 17] and Ni[10, 11]) sites with guest metal sites within these intermetallic structures, it is possible to suppress strong σ-adsorption and facilitate weaker π-adsorption of propylene, thereby promoting its desorption and preventing its further hydrogenation to propane. Our group has recently designed and constructed a supported NiSb catalyst, featuring well-ordered NiSb intermetallic nanoparticles uniformly anchored on the oxide support derived from Mg/Al-layered double hydroxides (LDHs)[11]. The optimized geometric structure and electronic local environment of electron-deficient Ni active sites, finely tuned by high-electronegativity p-block Sb guest atoms and acidic sites (Al^{3+} or cation vacancy)[18] on the support, facilitate the adsorption/activation of acetylene, as well as the desorption of ethylene, thus enhancing propyne semihydrogenation. However, few efforts have been devoted to

Received: August 6, 2024; **Revised:** September 20, 2024
Accepted: September 25, 2024

✉Address correspondence to Yueqiang Cao, yqcao@ecust.edu.cn; Xuezhi Duan, xzduan@ecust.edu.cn

https://doi.org/10.26599/CF.2024.9200020

designing and optimizing cost-effective Co-based catalysts for propyne semihydrogenation, despite their similarities to Ni-based catalysts, such as the unfilled d-electrons and good hydrogen activation[19].

In our latest work, we present a facile synthetic strategy for creating the intermetallic *P6$_3$/mmc* CoSb catalyst for configuration matching in propyne semihydrogenation, achieved through the structural conversion of LDHs precursors. The distinctive properties of electron-deficient Co sites, isolated by electron-abundant Sb sites, were comprehensively characterized using X-ray diffraction (XRD), high resolution transmission electron microscopy (HRTEM), and X-ray absorption spectroscopy (XAS). The catalytic performance of the CoSb intermetallic catalyst demonstrated a good propylene selectivity of up to ca. 97.0% with nearly complete propyne conversion, remarkably outperforming the reference Co catalyst. Additionally, temperature-programmed experiments and theoretical calculations were combined to elucidate the mechanisms behind the improved propyne semihydrogenation, which is attributed to the simultaneous promotion of propylene desorption and destabilization of the transition state for its further hydrogenation.

2 Results and discussion

As schematically shown in Fig. 1a, the Co/Sb/Mg/Al-LDH precursor was initially synthesized through a combination of anion exchange and thorough grinding with Sb powder. Afterwards, the CoSb intermetallic catalyst was precisely fabricated via a structural conversion process from presynthesized Co/Sb/Mg/Al quaternary LDHs at 900 °C in a hydrogen atmosphere. At such high temperatures, the antimony powder was melted into a liquid and mobile state, while the Co ions in Co/Mg/Al-LDHs were reduced to free Co atoms. As demonstrated in our previous study[20], the strong metallic bond interactions promote the bonding of free Sb and Co atoms, which spontaneously assemble into a stable and well-defined CoSb intermetallic compound. Supplementary Fig. S1 presents the XRD patterns for both the intermetallic CoSb and reference monometallic Co catalysts. Characteristic diffraction peaks observed at 19.1°, 31.7°, and 36.4° are associated with the (111), (220), and (311) planes of $MgAl_2O_4$ (JCPDS No. 21-1152), while peaks at 43.2° and 62.7° align well with the (200) and (220) planes of highly crystalline single-phase MgO (JCPDS No. 45-0946), respectively. Additionally, the XRD pattern of the CoSb intermetallic catalyst features seven distinct diffraction peaks at 31.8°, 34.7°, 44.2°, 46.9°, 57.5°, 60.2°, and 66.1°, corresponding to the (101), (002), (102), (110), (201), (103), and (202) crystal planes of high-purity hexagonal-phase CoSb (JCPDS No. 16-4409), respectively. In contrast, the monometallic Co catalyst clearly shows representative peaks at 44.2°, 51.7°, and 75.8°, which are related to the (111), (200), and (220) planes of face-centered cubic metallic Co (JCPDS No. 15-0806), respectively. These experimental XRD results are consistent with the theoretical simulations for CoSb and Co catalysts (Supplementary Fig. S2). The introduction of guest Sb significantly alters the original crystal morphology, as further evidenced by the Wulff construction in Supplementary Figs. S3 and S4. The CoSb(101) and Co(111) surfaces are identified as the energetically stable and predominantly exposed surfaces for CoSb and Co, respectively. Given the significant role of the predominantly exposed surface in propyne hydrogenation, density functional theory (DFT) calculations were performed on the Co(111) and CoSb(101) surfaces to investigate the differences in catalytic performance toward propyne semihydrogenation.

To thoroughly examine the microstructural features and properties of the synthesized Co and CoSb catalysts, high-angle annular dark field-scanning transmission electron microscopy (HAADF-STEM) and HRTEM characterizations were further employed. The randomly selected HAADF-STEM images reveal that the Co and CoSb nanoparticles are evenly distributed across the catalysts, with average sizes of 10.9 and 10.4 nm (Figs. 1b and 1c), respectively. The similar nanoparticle sizes enable us to investigate the effects of Sb sites on Co active sites while minimizing the influence of particle effects on propyne semihydrogenation. Figs. 1d and 1e display the representative HRTEM images and associated fast Fourier transform (FFT) patterns for Co and CoSb, respectively. The average lattice-fringe spacing in the line intensity curve (Fig. 1f), measured along the yellow arrow tagged in Fig. 1d, is 0.207 nm, corresponding to the (111) plane of *Fm*$\bar{3}$*m* monometallic Co phase[21]. Likewise, the measured lattice-fringe spacing in the HRTEM image of the CoSb catalyst is approximately 0.288 nm (Fig. 1g), matching well with the (101) plane of the *P6$_3$/mmc* CoSb intermetallic phase[22, 23]. The energy dispersive spectroscopy (EDS) line-scanning analysis shows that Co element is uniformly distributed within the individual particle with absence of Sb element (Fig. 1h), which is in strong agreement with the EDS mapping analyses shown in Fig. 2a and Supplementary Fig. S5. For the CoSb intermetallic catalyst, EDS line-scanning in Fig. 1i confirm a homogeneous distribution of Co and Sb throughout the randomly selected nanoparticle, aligning with the EDS mapping analyses in Fig. 2b and Supplementary Fig. S6. These results indicate the successful construction of the CoSb intermetallic catalyst with finely regulated Co sites.

The extended X-ray absorption fine structure (EXAFS) spectra were further utilized to elucidate the local coordination environment of the finely tuned Co sites in the CoSb intermetallic catalyst. The wavelet transform (WT)-EXAFS contour plots of both Co foil and Co catalyst reveal prominent scattering centers associated with the Co–Co coordination at approximately 2.0 Å of the *R*-axis (Fig. 3a). Conversely, the WT-EXAFS contour plot of the CoSb catalyst shows a distinct peak at around 2.5 Å, signifying Co–Sb bonding. Moreover, the Fourier transform (FT)-EXAFS spectrum at the Co K-edge for the CoSb catalyst exhibits a reduced intensity for the first nearest-neighbor coordination relative to the reference Co catalyst (Fig. 3b), indicating a diminished Co–Co coordination. Notably, the FT-EXAFS spectrum of CoSb shows a prominent scatting peak at approximately 2.40 Å assigned to the Co–Sb coordination, while the Co–Co peak approximately 2.10 Å is absent. In contrast, the Co–Co characteristic peak is clearly observed in the spectrum of the reference Co catalyst, indicating the presence of contiguous Co sites in monometallic Co catalyst. EXAFS oscillations in the K space for these Co-based catalysts, shown in Fig. 3c, reveal that the CoSb intermetallic catalyst displays much shorter periods and smaller amplitudes compared to Co foil and Co catalyst, indicating a longer Co–Sb coordination distance and a sparser coordination environment in the CoSb catalyst.

To unravel the electron transfer between Co and Sb in the CoSb intermetallic catalyst, the normalized X-ray absorption near edge structure (XANES) spectra at the Co K-edge were analyzed to elucidate the finely regulated electronic structure of Co sites in the CoSb catalyst. As observed in Fig. 3d, the photo-energy at the absorption edge and the white line intensity of the CoSb intermetallic catalyst are higher than those of monometallic Co

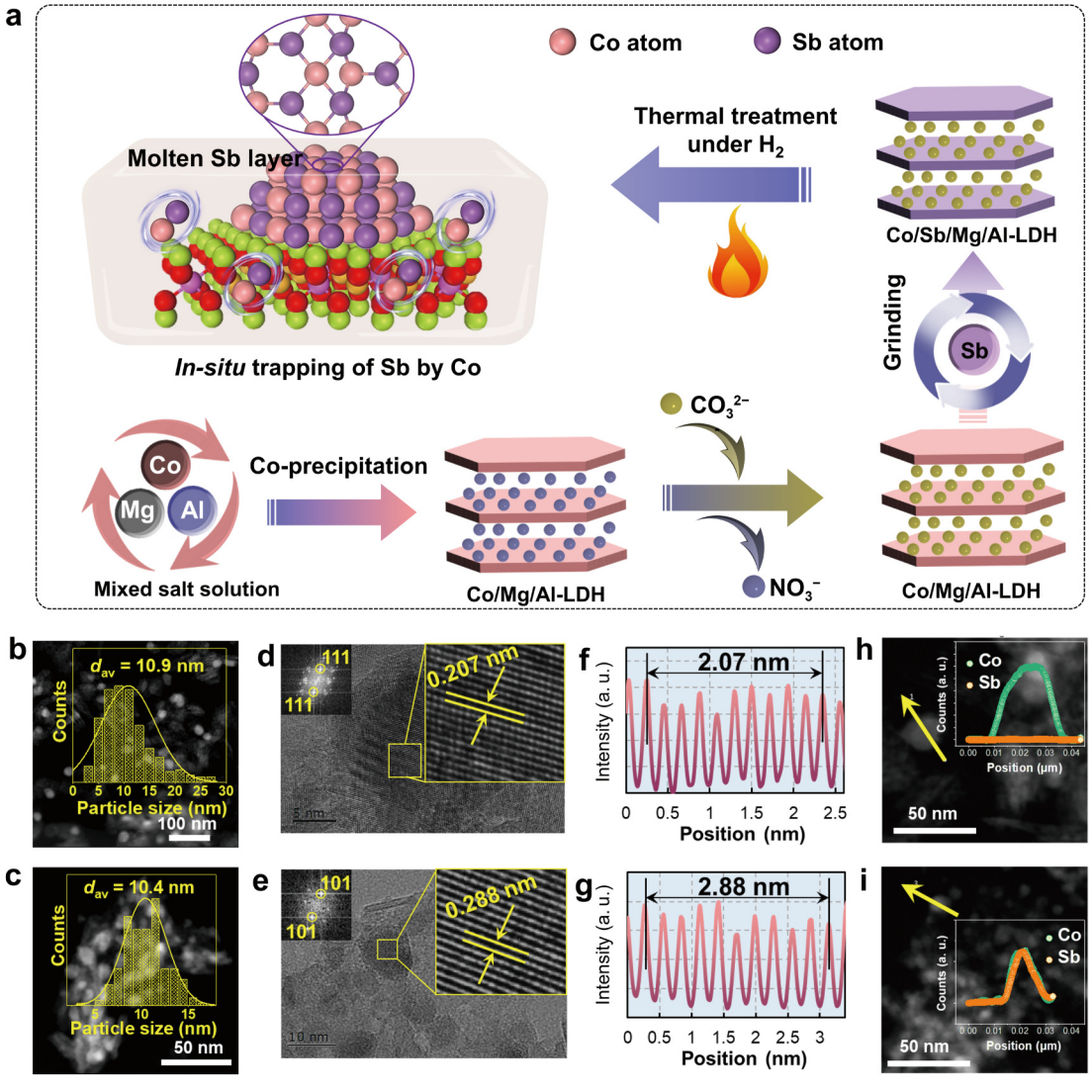

Fig. 1. Synthesis and structural characterization of CoSb catalyst. **a**, Schematic diagram illustrating the construction of the CoSb catalyst. **b**, **c**, **h**, **i**, HAADF-STEM images of Co (b and h) and CoSb (c and i) catalysts. Insets displayed in (b) and (c) are the associated particle size distribution histograms, and those shown in (h) and (i) are the associated EDS line-scanning curves. **d**, **e**, Representative HRTEM images and associated FFT patterns of Co (d) and CoSb (e) catalysts. **f**, **g**, Line intensity curves along directions denoted by the yellow arrows in (d) and (e).

catalyst and Co foil, indicating strong Co–Sb coupling and electron withdrawal from Co to Sb. X-ray photoelectron spectroscopy (XPS) spectra were subsequently utilized to determine the surface chemical valence states of these Co-based catalysts, providing detailed insights into their electronic structures. The Co 2p XPS spectrum of the as-synthesized Co catalyst displays a characteristic satellite peak at 786.4 eV, ascribed to multielectron excitation[15, 20] (Fig. 3e), with deconvoluted peaks located at 777.9 and 781.0 eV corresponding to Co^0 and Co^{2+} species, respectively. Conversely, the Co 2p peaks for the CoSb catalyst exhibit a significant positive shift of up to 0.60 eV toward higher binding energies compared to the Co catalyst. The Sb 4d XPS spectrum of the CoSb catalyst displays four distinct deconvoluted peaks attributed to Sb^0 and Sb^{3+} species (Fig. 3e), which are shifted to much lower binding energies relative to those in reference monometallic Sb[20, 24]. These shifts indicate a noticeable charge withdrawal from Co to neighboring Sb in the CoSb intermetallic structure, driven by the higher electron-withdrawing ability of Sb compared to Co. It should be emphasized that the presence of Co^{2+} and Sb^{3+} species is likely associated with sample re-oxidation during the *ex-situ* experiments[13, 20]. Further insights into the electronic properties of the CoSb intermetallic compound were obtained from theoretical calculations. The Bader charge density difference contour for CoSb(101) intermetallic surface indicates the noticeable electron withdrawal from Co to Sb (Supplementary Fig. S7), consistent with the XANES and XPS findings. Additionally, the density of states curves (Supplementary Fig. S8) reveal that the d-band of Co atoms overlaps with the p-band of Sb atoms within CoSb intermetallic structure, indicating significant hybridization and electron withdrawal from Co to Sb.

The catalytic efficiency of the CoSb catalyst featuring finely regulated Co sites was further assessed for propyne semihydrogenation with excess propylene and compared to a reference Co catalyst. Figs. 4a and 4b, Supplementary Fig. S9, and Tables S1 and S2 show the conversion of propyne as well as the

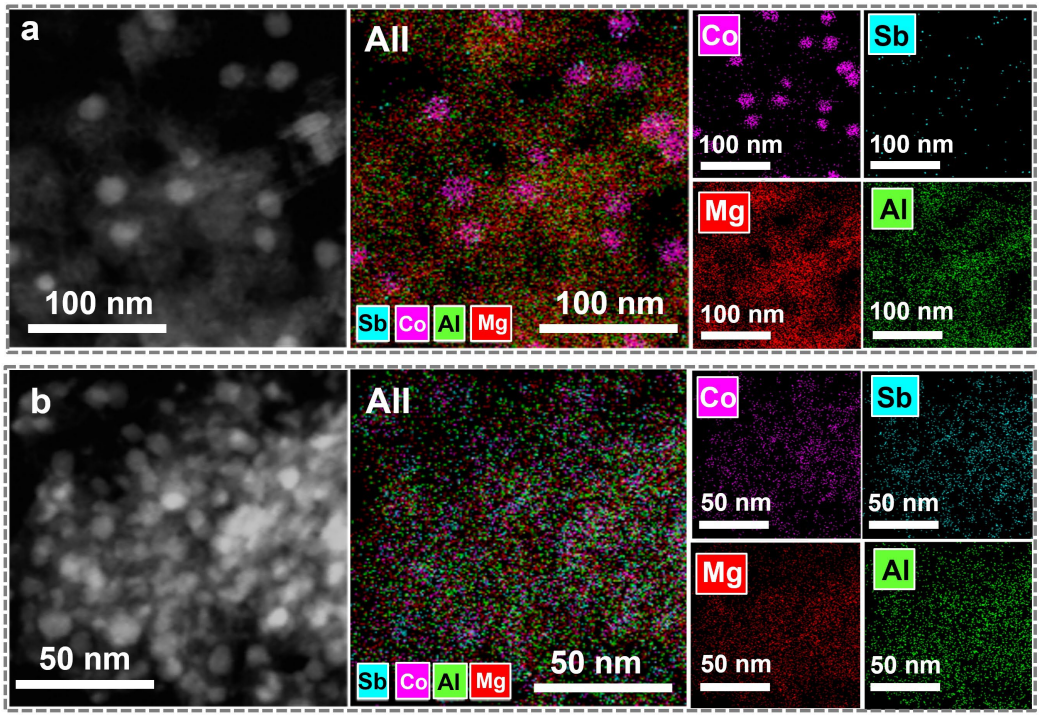

Fig. 2. Morphology and element distribution of the CoSb intermetallic catalyst. **a**, **b**, HAADF-STEM images of Co (a) and CoSb (b) catalysts along with corresponding EDS mapping analyses.

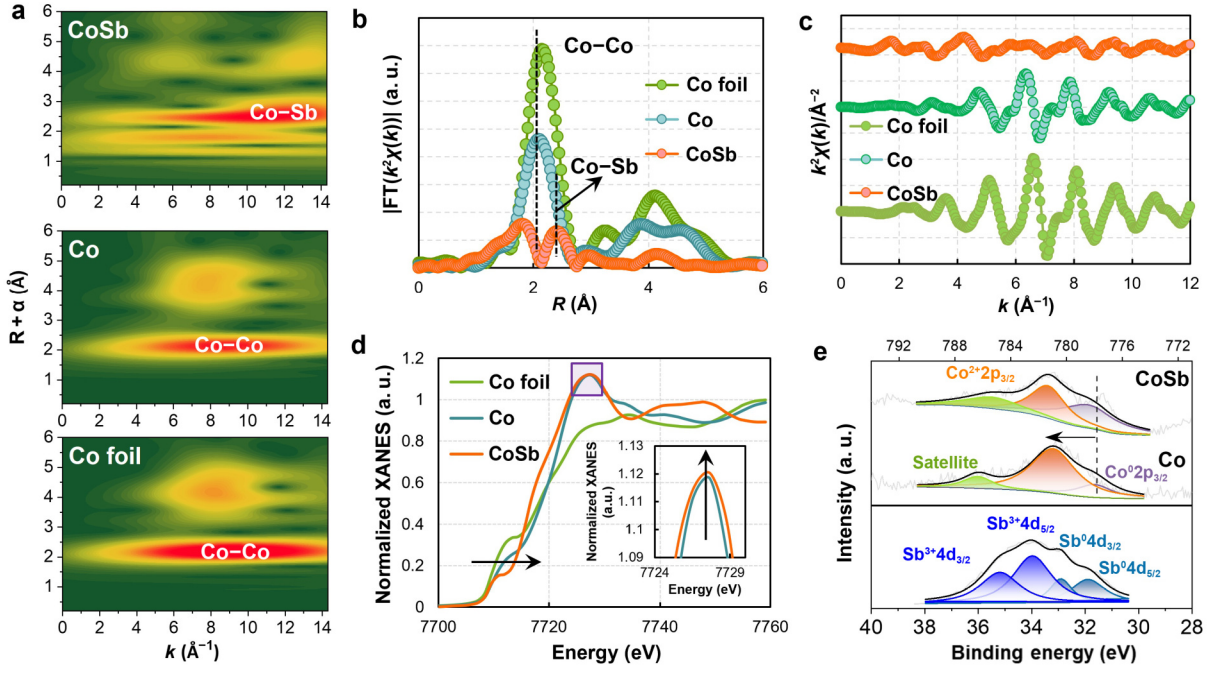

Fig. 3. Structure properties of CoSb intermetallic catalyst. **a**, WT-EXAFS contours at the Co K-edge for Co foil, Co, and CoSb catalysts. **b**, Fourier transforms of the experimental EXAFS spectra at the Co K-edge for Co foil, Co, and CoSb catalysts. **c**, EXAFS oscillation functions at the Co K-edge for Co foil, Co, and CoSb catalysts. **d**, Normalized XANES spectra at Co K-edge of Co foil, Co, and CoSb catalysts. **e**, XPS spectra of Co 2p and Sb 4d for Co and CoSb catalysts.

selectivity toward propylene and propane for both catalysts. The Co catalyst, with its continuous Co sites, shows higher activity but significantly lower propylene selectivity throughout the temperature range. Notably, the negative selectivity toward propylene on the reference Co catalyst suggests the further hydrogenation of propylene component present in the feed gas. Conversely, the CoSb catalyst exhibits relatively lower hydrogenation activity within such temperature range but maintains a high propylene selectivity of around 97.0%, attributed to the isolation of electron-deficient host Co sites by guest Sb sites. To further examine the excellent propylene selectivity of the CoSb catalyst, we performed propylene hydrogenation tests over both the monometallic Co and

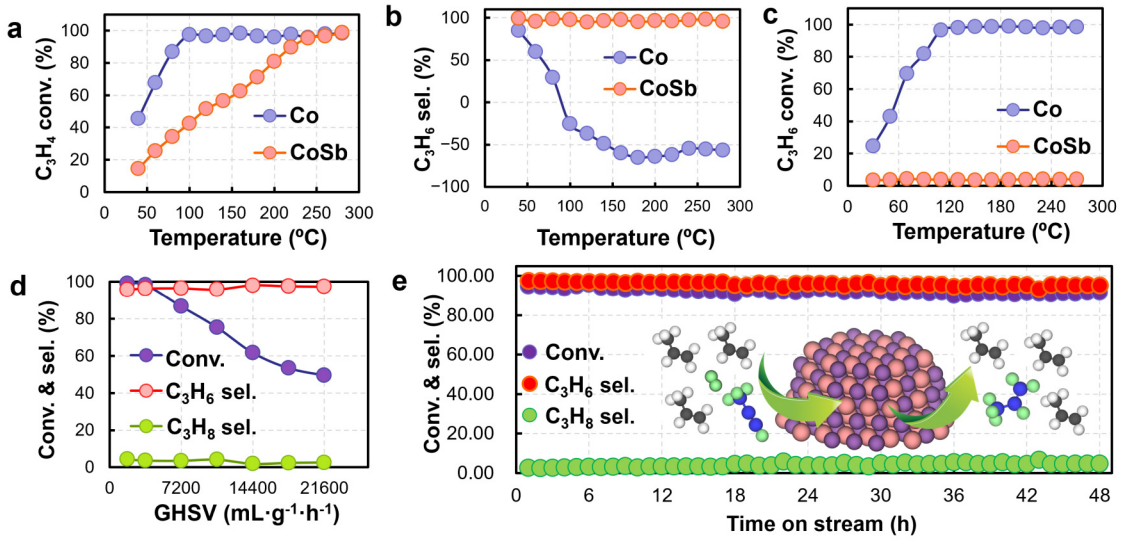

Fig. 4. Catalytic performance for propyne selective hydrogenation. **a**, **b**, C_3H_4 conversion (a) and C_3H_6 selectivity (b) as a function of reaction temperature. **c**, Temperature-dependent propylene hydrogenation over the Co and CoSb catalysts. **d**, Catalytic performance of the CoSb catalyst under various space velocities. **e**, Long-term durability stability assessment for the CoSb catalyst.

intermetallic CoSb catalysts. As depicted in Fig. 4c and Supplementary Table S3, the propylene conversion over the CoSb catalyst is remarkably lower than those over the Co catalyst across the entire temperature range, underscoring its ability to effectively suppress propylene hydrogenation.

The catalytic performances of the Co and CoSb catalysts were further evaluated under different gas flow rates at 240 °C (Fig. 4d, Supplementary Fig. S10, and Tables S4 and S5). The propyne conversion over the reference Co catalyst decreased slightly from 99.1% to 75.9% as the gas hourly space velocity (GHSV) increased from 1.8×10^3 to 2.16×10^4 mL·g^{-1}·h^{-1}. Concurrently, the selectivity toward desired propylene product increased from −55.7% to 33.8%, while propane selectivity fell from 155.7% to 66.2% with the increased GHSV (from 1.8×10^3 to 2.16×10^4 mL·g^{-1}·h^{-1}). Notably, the CoSb catalyst displayed consistent propylene selectivity around 95.0% across the GHSV range, demonstrating its stable catalytic performance regardless of contact time. The long-term durability stability for the CoSb intermetallic catalyst in excess propylene, illustrated in Fig. 4e and Supplementary Table S6, reveals that the propyne conversion remains steady at 93.0% over 48 h, with propylene selectivity maintained at 97.0% without noticeable decline under the reaction conditions, outperforming previously reported catalysts for propyne hydrogenation (Supplementary Table S7). Structural analyses of the used CoSb catalyst were performed to assess any potential changes in the intermetallic phase during the long-term durability stability experiment. The XRD pattern of the used CoSb catalyst clearly shows the presence of the *P6$_3$/mmc* CoSb intermetallic phase with no formation of other phases (Supplementary Fig. S11). Furthermore, the HAADF-STEM EDS mapping and line-scanning analyses indicate a uniform distribution of Co and Sb within the randomly selected nanoparticles (Supplementary Figs. S12 and S13). These findings strongly suggest the stable CoSb intermetallic structure during the propyne hydrogenation.

To explore the origin for the differences in propyne hydrogenation activity on the intermetallic CoSb and reference Co catalysts, the adsorption configurations of propyne on the Co(111) and CoSb(101) surfaces were further calculated (Supplementary Figs. S14 and S15). Propyne is strongly bound to the four-hollow Co sites on the Co(111) surface via a σ-adsorption mode with an adsorption energy of −2.61 eV. However, on the CoSb(101) surface, propyne stably adsorbs at the single Co site via a π-adsorption mode with a significantly lower adsorption energy of −0.82 eV, which is consistent with Bader charge analysis (Supplementary Fig. S16). This is mainly due to the strong repulsion between high electron density of the carbon–carbon triple bond in the electrophilic propyne and the electron-rich Sb sites[11, 20, 25], thereby significantly weakening the adsorption/activation of propyne and reducing its hydrogenation activity at low reaction temperatures.

The C_3H_6-temperature programmed desorption (TPD) analysis was conducted to provide insights into the specific adsorption and desorption behavior of target propylene product on the optimized Co sites within the CoSb catalyst. As depicted in Fig. 5a, the C_3H_6-TPD curve for the CoSb catalyst shows an obvious desorption peak at 174.5 °C, much lower than the peaks observed for the reference Co catalyst at 219.6 and 261.0 °C. This indicates that propylene has a reduced adsorption on the isolated Co sites modified by Sb. To explore the origin of enhanced propylene semihydrogenation, adsorption configurations of propylene on Co(111) and CoSb(101) surfaces were visualized and the results are shown in Supplementary Figs. S17 and S18. C_3H_6 is found to strongly adsorb at the three-hollow site on the Co(111) surface via a σ-adsorption mode with an adsorption energy of −0.93 eV. Conversely, on the CoSb(101) surface, propylene binds to a single Co site via a π-adsorption mode with a lower adsorption energy of −0.48 eV. This is in good agreement with the above-mentioned C_3H_6-TPD results. Bader charge analysis demonstrates that the electron withdrawal from the Co(111) surface to the adsorbed propylene is 0.30 e, considerably higher than the 0.17 e seen for the CoSb(101) surface (Fig. 5b). This aligns with the higher adsorption energy found on the Co(111) surface. The weak π-adsorption of propylene could be attributed to the electronic interaction between C atoms of propylene and surface Co atoms, as suggested by the hybridization

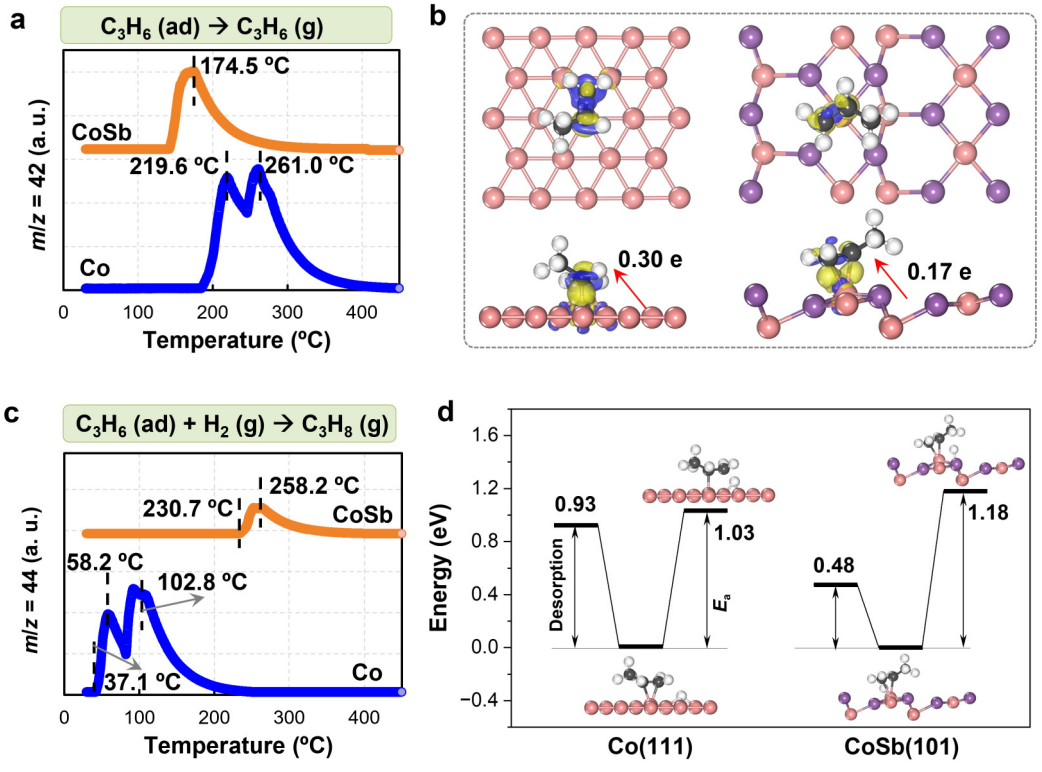

Fig. 5. Adsorption/desorption and hydrogenation behaviors. **a**, C_3H_6-TPD curves of Co and CoSb catalysts. **b**, Top and front views of the propylene adsorbed on Co(111) and CoSb(101) surfaces, along with the associated charge density distributions based on Bader charge analysis. The yellow and blue isosurfaces indicate electron density depletion and accumulation, respectively. **c**, TPSR curves for the hydrogenation of preadsorbed propylene on Co and CoSb catalysts. **d**, Energy barriers for the propylene desorption versus hydrogenation on Co(111) and CoSb(101) surfaces.

of C 2p with Co 3d orbitals (Supplementary Fig. S19). These findings indicate that the CoSb intermetallic catalyst offers a promising benchmark with a well-defined geometric and optimized electronic structure, effectively matching the target adsorption configuration of propylene product both energetically and kinetically.

Temperature-programmed surface reaction (TPSR) tests were conducted to evaluate the exceptional ability of the CoSb catalyst in inhibiting the over-hydrogenation of propyne. Fig. 5c shows the TPSR curves for propylene hydrogenation over both Co and CoSb catalysts. The propylene hydrogenation initiates at 37.1 °C on the monometallic Co catalyst, accompanied by two visible desorption peaks at 58.2 and 102.8 °C, which are much lower than the initiation temperature observed for the CoSb catalyst, which starts at 230.7 °C. In addition, the intensity of desorption peak in the TPSR curve of the CoSb catalyst is significantly weaker compared to the Co catalyst, indicating a reduced tendency for propylene hydrogenation on the CoSb catalyst. This weaker propylene adsorption on the CoSb catalyst would facilitate the propylene desorption rather than its further hydrogenation to undesired propane product. As illustrated in Fig. 5d, on the Co(111) surface with contiguous Co sites, the energy barrier for hydrogenating C_3H_6 to a C_3H_7 intermediate is 1.03 eV, comparable to the desorption energy (0.93 eV). This similarity suggests a potential for lower propylene selectivity due to minimal suppression of over-hydrogenation, aligning with the higher selectivity for undesired propane production over the reference Co catalyst (Supplementary Fig. S9). In contrast, on the CoSb(101) surface featuring isolated Co sites, the desorption energy for propylene (0.48 eV) is much lower than its further hydrogenation energy barrier (1.18 eV), indicating the desorption of propylene is kinetically more favorable than its further hydrogenation[12, 26].

3 Conclusions

In this study, the CoSb intermetallic catalyst with a precisely defined atomic structure was constructed via the structural conversion of an LDH precursor. The formation of *P6₃/mmc* CoSb intermetallic phase was evidenced by detailed structure analyses, including XRD, HAADF-STEM, and XAS. Catalytic evaluations demonstrate that this CoSb intermetallic catalyst with well-defined geometric and optimized electronic structure achieves approximately 97.0% selectivity for propylene at near-complete propyne conversion, significantly surpassing the performance of the reference Co catalyst. TPSR and C_3H_6-TPD measurements, combined with theoretical calculations, reveal that the excellent propylene selectivity originates from the kinetically preferred desorption of propylene as opposed to its further hydrogenation to undesired propane on the isolated Co active sites modified by Sb. These findings presented in this work indicate that cost-effective Co catalysts, precisely tuned by Sb, could serve as efficient alternatives for the selective hydrogenation of propyne and potentially other substrates.

4 Experimental

4.1 Materials and synthesis

Cobaltous nitrate hexahydrate, magnesium nitrate hexahydrate, and

aluminum nitrate nonahydrate were sourced from Sinopharm Chemical Reagent Co., Ltd. Additional chemicals, including sodium carbonate, sodium hydroxide, and antimony powder, were obtained from Aladdin. The presynthesized Co/Mg/Al-LDHs precursor was prepared using a straightforward coprecipitation technique, as previously reported by our research group[20]. The Co/Mg/Al-LDHs was then reduced in a 50 vol.% H_2/Ar atmosphere at 900 °C for 3 h to yield the reference Co catalyst. The precursor for the CoSb intermetallic catalyst was prepared by thoroughly mixing Co/Mg/Al-LDHs with Sb powder at an Sb/Co molar ratio of 1.0. This mixture was subsequently treated in a 50 vol.% H_2/Ar atmosphere at 900 °C for 3 h to yield the CoSb intermetallic catalyst, labeled as CoSb.

4.2 Characterizations of the materials

XRD data for the Co and CoSb catalysts were recorded using a D8 ADVANCE diffractometer with Cu Kα radiation operating at 40 kV and 40 mA. HRTEM and HAADF-STEM results were acquired using a JEOL JEM-2010 F transmission electron microscope. XPS spectra were collected with a Thermo Scientific ESCALAB 250xi system with Al Kα radiation. The electronic binding energies of the Co-based catalysts were calibrated using the C 1s peak (284.6 eV) as a reference standard. XAFS measurements at the Co K-edge (7709 eV) were conducted at the BL14W1 XAFS beamline of the Shanghai Synchrotron Radiation Facility.

TPSR experiments for propylene hydrogenation were carried out in a quartz U-tube reactor, using an online mass spectrometer (LCD200M, TILON) for the detection of gas-phase components. Typically, 100 mg of Co-based catalyst sample was treated at 900 °C for 3 h under a 50 vol.% H_2/Ar mixture flowing at 30 mL·min^{-1}, then cooled to ambient temperature under Ar. Subsequently, a 20 vol.% C_3H_6/Ar mixture was introduced at 20 mL·min^{-1} and maintained for 1 h. The reactor was then flushed with pure Ar at a gas flow rate of 30 mL·min^{-1} for 6 h. Following this, 5 vol.% H_2/Ar was introduced at 10 mL·min^{-1}. Once the mass spectrometer signal stabilized, the Co-based catalyst sample was heated from ambient temperature to 500 °C at a heating rate of 10 °C·min^{-1}, with desorbed species were monitored via the above-mentioned mass spectrometry.

For the C_3H_6-TPD measurements, the Co-based catalyst sample was pretreated similarly to the TPSR experiments. It was then exposed to 20 vol.% C_3H_6/Ar at a gas flow rate of 30 mL·min^{-1} for 1 h, followed by purging with pure Ar to eliminate residual gas-phase C_3H_6. The C_3H_6-TPD curves were obtained by heating the Co-based catalyst sample from ambient temperature to 500 °C at a heating rate of 10 °C·min^{-1}.

4.3 Propyne hydrogenation test

Catalytic performance was assessed using a stainless-steel tubular reactor equipped with a three-stage temperature-variable furnace. Approximately 500 mg of Co-based catalyst sample was placed in the steady-state temperature zone of the fixed-bed reactor and treated under 50 vol.% H_2/Ar flow at 30 mL·min^{-1} at 900 °C for 3 h. Once cooled to the target reaction temperature, a gas mixture consisting of 1 vol.% propyne, 5 vol.% propylene, 5 vol.% hydrogen, and the remainder Ar, was fed into the reactor at a 30 mL·min^{-1} flow rate. Continuous real-time monitoring of the inlet and outlet stream compositions was performed with a Micro GC Fusion gas analyzer (INFICON) equipped with a TCD. The calculation of propyne conversion and product selectivity was carried out as follows:

$$C_3H_4\ \text{conversion} = \frac{C_3H_4(\text{inlet}) - C_3H_4(\text{outlet})}{C_3H_4(\text{inlet})} \times 100\%$$

$$S(C_3H_6) = \left\{1 - \frac{C_3H_8(\text{outlet}) - C_3H_8(\text{inlet})}{C_3H_4(\text{inlet}) - C_3H_4(\text{outlet})}\right\} \times 100\%$$

$$S(C_3H_8) = \frac{C_3H_8(\text{outlet}) - C_3H_8(\text{inlet})}{C_3H_4(\text{inlet}) - C_3H_4(\text{outlet})} \times 100\%$$

4.4 DFT calculations

All DFT calculations were performed using the highly regarded Vienna Ab initio Simulation Package (VASP)[27–29], employing plane wave basis sets and projected-augmented wave pseudopotentials[30]. The generalized gradient approximation of Perdew-Burke-Ernzerhof (PBE)[31] was applied to explicitly define the exchange-correlation functionals. The Co(111) surface was simulated using $p(3 \times 3)$ supercells with four layers, and the CoSb(101) and CoSb(102) surfaces were constructed with four layers in $p(2 \times 3)$ supercells. The bottom two layers were held fixed, and the remaining layers were permitted to relax at the bulk lattice sites. The CoSb(100) surface was represented with two layers in $p(3 \times 3)$ supercells, with the bottom layer immobilized and the other allowed to relax at the bulk lattice sites. A vacuum layer measuring 20 Å in thickness was included between the periodically repeated slabs to avoid interactions with neighboring cells. The transition states for the elementary steps of propylene hydrogenation were determined using the dimer method[32] and verified through vibrational frequency analysis to ensure the presence of only one imaginary frequency. Bader charge analysis[33] was conducted to ascertain the specific atomic electronic charges, which helped in exploring the electronic interactions between Co and Sb, as well as between adsorbed species and the metal surfaces.

References

[1] Gu, J.; Jian, M. Z.; Huang, L.; Sun, Z. H.; Li, A. W.; Pan, Y.; Yang, J. Z.; Wen, W.; Zhou, W.; Lin, Y. et al. Synergizing metal-support interactions and spatial confinement boosts dynamics of atomic nickel for hydrogenations. *Nat. Nanotechnol.* **2021**, *16*, 1141–1149.

[2] Wang, A. Q.; Li, J.; Zhang, T. Heterogeneous single-atom catalysis. *Nat. Rev. Chem.* **2018**, *2*, 65–81.

[3] Gao, R. J.; Xu, J. S.; Wang, J.; Lim, J.; Peng, C.; Pan, L.; Zhang, X. W.; Yang, H. M.; Zou, J. J. Pd/Fe_2O_3 with electronic coupling single-site Pd–Fe pair sites for low-temperature semihydrogenation of alkynes. *J. Am. Chem. Soc.* **2022**, *144*, 573–581.

[4] Liu, Y. N.; Zhao, J. Y.; Feng, J. T.; He, Y. F.; Du, Y. Y.; Li, D. Q. Layered double hydroxide-derived Ni–Cu nanoalloy catalysts for semi-hydrogenation of alkynes: Improvement of selectivity and anti-coking ability via alloying of Ni and Cu. *J. Catal.* **2018**, *359*, 251–260.

[5] Cao, Y. Q.; Sui, Z.; Zhu, Y. A.; Zhou, X. G.; Chen, D. Selective hydrogenation of acetylene over Pd–In/Al_2O_3 catalyst: Promotional effect of indium and composition-dependent performance. *ACS Catal.* **2017**, *7*, 7835–7846.

[6] Yan, K. L.; Ge, X. H.; Li, W. H.; Liang, Y. J.; Xiong, W. J.; Zhang, J.; Qian, G.; Chen, D.; Cao, Y. Q.; Zhou, X. G. et al. Regulation of a Ni_3Sn_2 intermetallic catalyst using highly dispersed Pd species to boost propyne semi-hydrogenation. *J. Mater. Chem. A* **2024**, *12*, 16482–16490.

[7] Yuwen, Q.; Yan, K. L.; Ge, X. H.; Qian, G.; Zhang, J.; Cao, Y. Q.;

Zhou, X. G.; Duan, X. Z. Atomically dispersed palladium to enhance the propyne semihydrogenation over CeO_2 catalysts. *Ind. Eng. Chem. Res.* **2023**, *62*, 16280–16290.

[8] Chu, M. Y.; Pan, Q.; Bian, W. Y.; Liu, Y.; Cao, M. H.; Zhang, C. Y.; Lin, H. P.; Zhang, Q.; Xu, Y. Strong metal-support interaction between palladium and gallium oxide within monodisperse nanoparticles: Self-supported catalysts for propyne semi-hydrogenation. *J. Catal.* **2021**, *395*, 36–45.

[9] Ge, X. H.; Cao, Y. Q.; Yan, K. L.; Li, Y. R.; Zhou, L. H.; Dai, S.; Zhang, J.; Gong, X. Q.; Qian, G.; Zhou, X. G. et al. Increasing the distance of adjacent palladium atoms for configuration matching in selective hydrogenation. *Angew. Chem., Int. Ed.* **2022**, *61*, e202215225.

[10] Ge, X. H.; Yin, J.; Ren, Z. H.; Yan, K. L.; Jing, Y. D.; Cao, Y. Q.; Fei, N. N.; Liu, X.; Wang, X. N.; Zhou, X. G. et al. Atomic design of alkyne semihydrogenation catalysts via active learning. *J. Am. Chem. Soc.* **2024**, *146*, 4993–5004.

[11] Xi, J. H.; Yan, K. L.; Zhu, N. C.; Ge, X. H.; Yuwen, Q.; Chen, M. M.; Jiang, H.; Cao, Y. Q.; Zhou, X. G.; Duan, X. Z. Ni active sites isolated by antimony toward enhanced propyne semihydrogenation. *AIChE J.* **2024**, *70*, e18416.

[12] Feng, Q. C.; Zhao, S.; Wang, Y.; Dong, J. C.; Chen, W. X.; He, D. S.; Wang, D. S.; Yang, J.; Zhu, Y. M.; Zhu, H. L. et al. Isolated single-atom Pd sites in intermetallic nanostructures: High catalytic selectivity for semihydrogenation of alkynes. *J. Am. Chem. Soc.* **2017**, *139*, 7294–7301.

[13] Cao, Y. Q.; Zhang, H.; Ji, S. F.; Sui, Z.; Jiang, Z.; Wang, D. S.; Zaera, F.; Zhou, X. G.; Duan, X. Z.; Li, Y. D. Adsorption site regulation to guide atomic design of Ni–Ga catalysts for acetylene semi-hydrogenation. *Angew. Chem., Int. Ed.* **2020**, *59*, 11647–11652.

[14] Huang, F.; Peng, M.; Chen, Y. L.; Cai, X. B.; Qin, X. T.; Wang, N.; Xiao, D. Q.; Jin, L.; Wang, G. Q.; Wen, X. D. et al. Low-temperature acetylene semi-hydrogenation over the Pd_1–Cu_1 dual-atom catalyst. *J. Am. Chem. Soc.* **2022**, *144*, 18485–18493.

[15] Ge, X. H.; Ren, Z. H.; Cao, Y. Q.; Liu, X.; Zhang, J.; Qian, G.; Gong, X. Q.; Chen, L. W.; Zhou, X. G.; Yuan, W. K. et al. Enhanced acetylene semihydrogenation on a subsurface carbon tailored Ni–Ga intermetallic catalyst. *J. Mater. Chem. A* **2022**, *10*, 19722–19731.

[16] Zhang, W. Q.; Zhang, X. B.; Wang, J. Y.; Ghosh, A.; Zhu, J.; LiBretto, N. J.; Zhang, G. H.; Datye, A. K.; Liu, W.; Miller, J. T. Bismuth-modulated surface structural evolution of Pd_3Bi intermetallic alloy catalysts for selective propane dehydrogenation and acetylene semihydrogenation. *ACS Catal.* **2022**, *12*, 10531–10545.

[17] Wang, M. L.; Liang, L. L.; Liu, X.; Sun, Q.; Guo, M. R.; Bai, S. X.; Xu, Y. Selective semi-hydrogenation of alkynes on palladium-selenium nanocrystals. *J. Catal.* **2023**, *418*, 247–255.

[18] He, Y. F.; Fan, J. X.; Feng, J. T.; Luo, C. Y.; Yang, P. F.; Li, D. Q. Pd nanoparticles on hydrotalcite as an efficient catalyst for partial hydrogenation of acetylene: Effect of support acidic and basic properties. *J. Catal.* **2015**, *331*, 118–127.

[19] Yang, Y. S.; Rao, D. M.; Chen, Y. D.; Dong, S. Y.; Wang, B.; Zhang, X.; Wei, M. Selective hydrogenation of cinnamaldehyde over Co-based intermetallic compounds derived from layered double hydroxides. *ACS Catal.* **2018**, *8*, 11749–11760.

[20] Ge, X. H.; Dou, M. Y.; Cao, Y. Q.; Liu, X.; Yuwen, Q.; Zhang, J.; Qian, G.; Gong, X. Q.; Zhou, X. G.; Chen, L. W. et al. Mechanism driven design of trimer Ni_1Sb_2 site delivering superior hydrogenation selectivity to ethylene. *Nat. Commun.* **2022**, *13*, 5534.

[21] Dietrich, P. J.; Akatay, M. C.; Sollberger, F. G.; Stach, E. A.; Miller, J. T.; Delgass, W. N.; Ribeiro, F. H. Effect of Co loading on the activity and selectivity of PtCo aqueous phase reforming catalysts. *ACS Catal.* **2014**, *4*, 480–491.

[22] Park, M. G.; Song, J. H.; Sohn, J. S.; Lee, C. K.; Park, C. M. Co–Sb intermetallic compounds and their disproportionated nanocomposites as high-performance anodes for rechargeable Li-ion batteries. *J. Mater. Chem. A* **2014**, *2*, 11391–11399.

[23] Ma, C. Q.; Zhang, H. F.; Xia, J.; Zhu, X. J.; Qu, K. Y.; Feng, F. K.; Han, S. M.; He, C. H.; Ma, X.; Lin, G. et al. Screening of intermetallic compounds based on intermediate adsorption equilibrium for electrocatalytic nitrate reduction to ammonia. *J. Am. Chem. Soc.* **2024**, *146*, 20069–20079.

[24] Fan, G. L.; Xu, W. C.; Li, J. H.; Chen, J. L.; Yu, M.; Ni, Y. X.; Zhu, S. L.; Su, X. C.; Cheng, F. Y. Nanoporous NiSb to enhance nitrogen electroreduction via tailoring competitive adsorption sites. *Adv. Mater.* **2021**, *33*, 2101126.

[25] Melloni, G.; Modena, G.; Tonellato, U. Relative reactivities of carbon-carbon double and triple bonds toward electrophiles. *Acc. Chem. Res.* **1981**, *14*, 227–233.

[26] Ge, X. H.; Jing, Y. D.; Fei, N. N.; Yan, K. L.; Liang, Y. J.; Cao, Y. Q.; Zhang, J.; Qian, G.; Li, L. N.; Jiang, H. et al. Embedding single Pd atoms on NiGa intermetallic surfaces for efficient and selective alkyne hydrogenation. *Angew. Chem., Int. Ed.* **2024**, *5*, e202410979.

[27] Kresse, G.; Furthmüller, J. Efficiency of *ab-initio* total energy calculations for metals and semiconductors using a plane-wave basis set. *Comput. Mater. Sci.* **1996**, *6*, 15–50.

[28] Kresse, G.; Furthmüller, J. Efficient iterative schemes for *ab initio* total-energy calculations using a plane-wave basis set. *Phys. Rev. B* **1996**, *54*, 11169–11186.

[29] Kresse, G.; Joubert, D. From ultrasoft pseudopotentials to the projector augmented-wave method. *Phys. Rev. B* **1999**, *59*, 1758–1775.

[30] Blöchl, P. E. Projector augmented-wave method. *Phys. Rev. B* **1994**, *50*, 17953–17979.

[31] Perdew, J. P.; Burke, K.; Ernzerhof, M. Generalized gradient approximation made simple. *Phys. Rev. Lett.* **1996**, *77*, 3865–3868.

[32] Kästner, J.; Sherwood, P. Superlinearly converging dimer method for transition state search. *J. Chem. Phys.* **2008**, *128*, 014106.

[33] Tang, W.; Sanville, E.; Henkelman, G. A grid-based Bader analysis algorithm without lattice bias. *J. Phys.: Condens. Matter* **2009**, *21*, 084204.

Data availability

All data required to support the conclusions of this paper are included in the manuscript and/or the Supplementary Information. Further data related to this research can be requested from the corresponding author.

Acknowledgements

This work was financially supported by the National Key R&D Program of China (2022YFA1503804), the National Natural Science Foundation of China (22332003, 22478106 and 22408097), Shanghai Rising-star Program (23QA1401900), the Shanghai Science and Technology Innovation Action Plan (22JC1403800), the Program of Shanghai Academic/Technology Research Leader (21XD1421000), Young Elite Scientists Sponsorship Program by

CAST (2023QNRC001), the Fundamental Research Funds for the Central Universities, and the Postdoctoral Fellowship Program of CPSF (GZB20240222). This work was also supported by BL14W1, 13SSW, and User Experiment Assist System of SSRF.

Author contributions

X.G. was responsible for the experiments, theoretical calculations, data collection, and manuscript writing. Z.K. and N.F. assisted with catalytic testing. Y.C. and X.D. conceived the project, planned the research, supervised the experimental work, and edited the manuscript. H.J. and X.Z. assisted with data analysis and discussions.

Competing interests

The authors declare no conflicts of interest.

Additional information

Supplementary Information The online version contains supplementary material available at https://doi.org/10.26599/CF.2024.9200020.